

# SMDS-Net: Model Guided Spectral-Spatial Network for Hyperspectral Image Denoising

Fengchao Xiong, Jun Zhou, Jianfeng Lu, and Yuntao Qian

**Abstract**—Deep learning (DL) based hyperspectral images (HSIs) denoising approaches directly learn the nonlinear mapping between observed noisy images and underlying clean images. They normally do not consider the physical characteristics of HSIs, therefore making them lack of interpretability that is key to understand their denoising mechanism. In order to tackle this problem, we introduce a novel model guided interpretable network for HSI denoising. Specifically, fully considering the spatial redundancy, spectral low-rankness and spectral-spatial properties of HSIs, we first establish a subspace based multi-dimensional sparse model. This model first projects the observed HSIs into a low-dimensional orthogonal subspace, and then represents the projected image with a multidimensional dictionary. After that, the model is unfolded into an end-to-end network named SMDS-Net whose fundamental modules are seamlessly connected with the denoising procedure and optimization of the model. This makes SMDS-Net convey clear physical meanings, i.e., learning the low-rankness and sparsity of HSIs. Finally, all key variables including dictionaries and thresholding parameters are obtained by the end-to-end training. Extensive experiments and comprehensive analysis confirm the denoising ability and interpretability of our method against the state-of-the-art HSI denoising methods.

## I. INTRODUCTION

Hyperspectral images (HSIs) have enabled many practical applications such as pedestrian detection [4]–[6], object tracking [7], medical diagnosis [8] and more thanks to its material identification ability provided by numerous light-wavelength indexed bands. Because of narrow bands, limited sensitivity of sensors or their defects, and the interference of the imaging environment, the captured HSIs tend to be corrupted by noises. The degradation of HSIs brings many drawbacks in the exploitation of HSI and significantly decreases their utility as well. Therefore, HSI denoising is often needed as a critical preprocessing step to enhance the quality of HSIs.

HSI denoising can be generally considered as an ill-posed inverse problem that recovers underlying clean HSIs from the observed noisy ones. Domain knowledge is very important to tackle such problem. In the last few years, many researchers have made explicit hypothesis on the underlying physical characteristics and degradation process of HSIs and

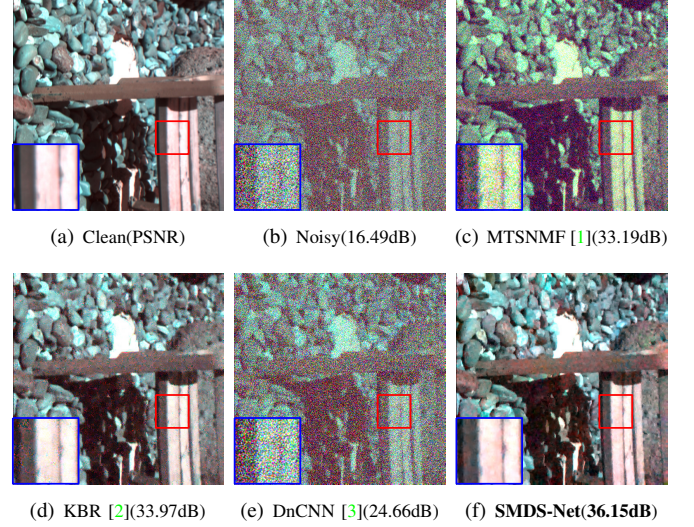


Fig. 1. Denoising results on the ICVL dataset with the noise variance between 0 and 95. The proposed SMDS-Net obtains the best quantitative and qualitative results.

introduced various prior structures, for example, nonlocal similarity, spectral low-rankness, spatial redundancy, spectral-spatial correlation, just to name a few. As important tools to model these structures, sparse coding [1], [9]–[13] and low-rank representations [11], [14], [15] are mostly investigated. Matrix based sparse/low-rank models evidently destroy the spectral-spatial structure of HSIs and require more parameters. For this reason, tensor-based sparse/low-rank representations are introduced and successfully employed in HSI denoising [2], [16]–[21]. These model-based methods are physically interpretable and easy to analyze but heavily depend on the effectiveness of hand-crafted priors, computational demanding iterative optimization and exhaustive hyperparameter tuning.

Inspired by the image representation and success of deep learning (DL) in HSI classification, some attempts have been made on deep convolutional neural networks (CNNs) for HSI denoising [22]–[28]. Instead of subjective physical assumption on the underlying HSIs, they directly learn the nonlinear end-to-end mapping between the noisy and clean HSIs. This normally required training on a large number of noisy-clean HSI pairs that unfortunately are very costly to acquire [29], [30]. The lack of data dramatically limits their generalization ability. Moreover, complicated network architectures also hinder deep analysis on the functionality of different modules and comprehensive understanding of the rationality behind their denoising mechanisms.

Given the above discussion, it is more preferable to design a

This work was supported in part by the 2030 National Key AI Program of China under Grant 2018AAA0100500 and the National Key Research and Development Program of China under Grant 2017YFB1300205 and 2018YFB0505000.

F. Xiong and J. Lu are with the School of Computer Science and Engineering, Nanjing University of Science and Technology, Nanjing 210094, P.R. China (Corresponding author: F. Xiong; fcxiong@njust.edu.cn).

J. Zhou is with the School of Information and Communication Technology, Griffith University, Nathan, Australia.

Y. Qian is with the College of Computer Science, Zhejiang University, Hangzhou 310027, China.

DL-based HSI denoising method that combines the advantages of both model-based and DL-based methods, i.e., the network is of high interpretability while supporting discriminative learning. To reach this goal, the spectral-spatial structure, low-rank and sparse structure priors and end-to-end learning are very important factors to be considered. In this paper, a model guided network is introduced for HSI denoising, which simultaneously considers all the above factors in a unified network. Specifically, our contributions are summarized as follows:

- Firstly, we propose a subspace based multi-dimensional sparse (SMDS) model for HSI denoising. SMDS firstly projects the high-dimensional HSIs into low-dimensional spectral subspace and exploits the spatial redundancy property of the projected image under the umbrella of multidimensional (MD) tensor sparse representation. In this way, SMDS is able to simultaneously capture the spectral low-rankness, spatial sparsity properties and spectral-spatial structure of HSIs with less parameters. Moreover, considering the spatial sparsity prior on the projected image also helps to reduce the number of cubes required for encoding.
- Secondly, by unfolding the denoising procedure and optimization algorithm of SMDS, an end-to-end interpretable deep neural network named SMDS-Net is obtained. As shown in Figure 2, SMDS-Net includes five stages, i.e. subspace projection, cube extraction, multi-dimensional sparse coding, cube aggregation and image reconstruction. Each stage has clear physical meaning, implying the interpretability of our network and facilitating generation ability with less parameters. To the best of our knowledge, this is the first time that low-rankness, sparsity and spectral-spatial structure were simultaneously taken into consideration in a unified end-to-end network for HSI denoising.
- Thirdly, extensive experiments with comprehensive analysis are provided for model verification and explanation. The impressive denoising results confirm the advantages of the SMDS-Net over other state-of-the-art model-based and DL-based methods. Moreover, a comprehensive analysis of the network is carried out to fully explain our network denoising mechanism.

The remainder of this paper is organized as follows. Section II introduces the recent works on HSI denoising. Section III presents the subspace based MD sparse model and its optimization algorithm. In Section IV, we unfold the optimization and denoising procedure of SMDS to yield the SMDS-Net for HSI denoising. Extensive experimental results and comprehensive analysis are presented in Section V. Finally, Section VI concludes the paper with future work.

## II. RELATED WORK

In this section, we review the most relevant work on HSI denoising. These work can be grouped into model based methods and deep learning based methods.

### A. Model Based Approaches

HSIs can be considered as a stack of 2D images along the spectral dimension. Therefore, traditional 2D image denoising methods such as K-SVD [31], Non-local means (NLM) [32] and BM3D [33] can be directly applied for HSI denoising in a band-wise manner. Band-wise methods ignore the spectral-spatial correlation in HSIs, leading to unsatisfactory denoising performance. To solve this problem, spectral-spatial methods model HSIs at the cube level to capture information in the 3D spectral-spatial domain. Typical examples include BM4D [34] and 3D NLM [35].

Several HSI denoising methods are based on sparse representation, in which predefined fixed dictionary are manually or analytically constructed based on sparse formulation of data. For example, Qian *et al.* extended 2D Discrete Wavelet Transformation (DWT) and 2D discrete Cosine Transformation (DCT) to 3D space and produced dictionary from 3D hyperspectral cubes [36]. Alternatively, dictionaries can be learned from training data, leading to more flexibility in handling various scenarios [1], [10], [12], [20], [37]. Moreover, structural sparse coding demonstrates its effectiveness by embedding the local and nonlocal similarity structures of HSIs into sparse coding [11], [36].

Besides sparsity, low-dimensional structures also exist in HSIs and can be depicted by low-rank approximation [2], [9], [21], [38]–[40] or low-rank decomposition [16], [41]–[45]. The spectral correlation among bands make the acquired spectrum essentially lie in a very low-dimensional spectral subspace [46]–[48] as exemplified by hyperspectral fusion [47] and reconstruction [46]. On the other hand, spatial low-rank structures in images can also be defined because of nonlocal spatial similarity. By clustering a number of band patches (cubes), the grouped patches show low-rank property [14], [45]. Recently, combining both spatial and spectral low-rank properties of HSIs is a new trend of HSI denoising. It can be realized by projecting the observed HSIs into spectral subspace and performing denoising in projected image [23], [29], [49]. Although these methods work well when the prior model assumptions match well with the HSIs to be processed, they normally require iterative numerical optimization which is computationally expensive.

### B. Deep Learning Based Approaches

Taking advantages of the image representation capability of deep learning, deep CNNs have been introduced for HSI denoising. Chang *et al.* [24] learned a series of multiple channels of 2D filters for the consideration of both spatial and spectral structures of HSIs. Yuan *et al.* [25] proposed multiscale spectral-spatial denoising through multi-scale feature extraction and multilevel feature representation using deep neural networks. To effectively extract the joint spectral-spatial information, Zhao *et al.* [27] and Maffei *et al.* [22] took current band and its  $K$  adjacent bands as input. Alternatively, structural spectral-spatial correlations in HSIs can also be extracted by 3D convolutions [26], [28]. Instead of directly operating on the original HSIs, noisy HSIs can be converted into low-dimensional HSIs before applying CNNs on the

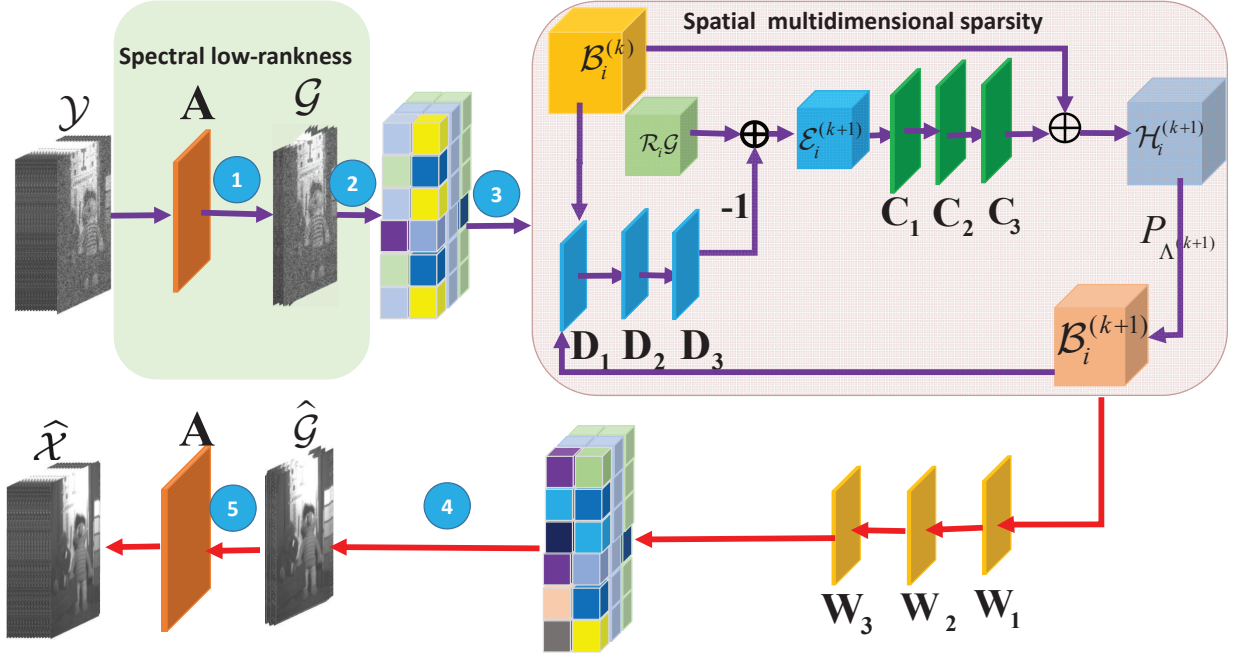


Fig. 2. The framework of SMDS-Net which has five stages connected with spatial sparsity and spectral low-rankness of HSIs. The observed noisy HSI  $\mathcal{Y}$  is first projected into a low-dimensional image  $\mathcal{G}$  with respect to learned subspace  $\mathbf{A}$  (①).  $\mathcal{G}$  is divided into a number of overlapped cubes (②), followed by MDS-Net which sparsely encodes a data cube under the framework of tensor (③). After that, each encoded cube is reconstructed and aggregated to yield estimated  $\hat{\mathcal{G}}$  (④). Finally, the network outputs the denoised image  $\hat{\mathcal{X}}$  using  $\mathbf{A}$  (⑤).

reduced images [23], [29]. Although these methods are able to recover the underlying image via training deep models on a large number of noisy-clean HSI pairs, they often ignore very important intrinsic prior structures inside the HSIs such as sparsity and low-rankness as mentioned previously. Instead, they perform denoising in a “black box” mechanism whose architecture is empirically determined in heuristic manner and exhausting trials, making further model improvement difficult. Therefore, interpretability of the actual functionality is a matter of concern.

### III. SMDS HSI DENOISING MODEL

In this section, we introduce the proposed subspace based multidimensional sparse model in detail.

#### A. Notations

In this paper, we represent a scalar by a lowercase letter, e.g.  $y$ ; a vector by a bold lowercase letter, e.g.  $\mathbf{y} \in \mathbb{R}^I$ ; a matrix by a bold capital letter, e.g.  $\mathbf{Y} \in \mathbb{R}^{I_1 \times I_2}$ ; and a tensor by a bold calligraphic letter, e.g.  $\mathcal{Y} \in \mathbb{R}^{I_1 \times I_2 \times \dots \times I_N}$ . The  $L_0$  norm of a tensor  $\mathcal{Y}$  is defined as the number of non-zero entries, i.e.,  $\|\mathcal{Y}\|_0 = \#\{\mathcal{Y}_{i_1, i_2, \dots, i_N} \neq 0\}$ . The  $L_1$  norm and Frobenius norm of  $\mathcal{Y}$  are respectively defined as  $\|\mathcal{X}\|_1 = \sum_{i_1} \sum_{i_2} \dots \sum_{i_N} |\mathcal{Y}_{i_1, i_2, \dots, i_N}|$ ,  $\|\mathcal{X}\|_F = \sqrt{\sum_{i_1} \sum_{i_2} \dots \sum_{i_N} (\mathcal{Y}_{i_1, i_2, \dots, i_N})^2}$ . The n-mode unfolding is the process of arranging all the n-mode vectors as columns of a matrix, denoted by  $\mathbf{Y}_{(n)}$ . The n-mode product of a tensor  $\mathcal{Y}$  and matrix  $\mathbf{U} \in \mathbb{R}^{J \times I_n}$  is written as  $\mathcal{Y} \times_n \mathbf{U}$  and computed by  $(\mathcal{Y} \times_n \mathbf{U})_{i_1 \dots i_{n-1} j i_{n+1} \dots i_N} = \sum_{i_n=1}^{I_n} \mathcal{Y}_{i_1 i_2 \dots i_N} u_{j i_n}$ .

#### B. Model Formulation

Given an HSI  $\mathcal{Y}$  with  $H \times W$  pixels and  $B$  bands corrupted by additive zero-mean Gaussian noise  $\mathcal{N}$ , the observation model can be represented as

$$\mathcal{Y} = \mathcal{X} + \mathcal{N} \quad (1)$$

where  $\mathcal{X}$  is the clean HSI to be estimated. This problem is an ill-posed inverse problem and prior knowledge on  $\mathcal{X}$  is very important to solve the problem. Specifically, we consider spatial sparsity and spectral low-rankness prior to model  $\mathcal{X}$ .

**Spectral low-rankness:** As stated in [50], the acquired spectra in fact lie in a low-dimensional subspace, i.e.,

$$\mathcal{X} = \mathcal{G} \times_3 \mathbf{A} \quad (2)$$

Here  $\mathbf{A} = [\mathbf{a}_1, \dots, \mathbf{a}_R] \in \mathbb{R}^{B \times R}$  is the spectral subspace spanned by  $R$  bases with  $R$  far less than  $B$  and  $\mathcal{G} \in H \times W \times R$  is the representation tensor with respect to  $\mathbf{A}$ . In general,  $\mathbf{A}$  can be obtained by many approaches, for example, unmixing and SVD decomposition on the unfolded  $\mathcal{Y}$  along spectral models. Since an orthogonal subspace shares many merits such as disentangling the correlation among bands and encouraging decorrelation among the components of  $\mathcal{G}$  [14], [29], [49], we choose a set of orthonormal bases, i.e.,  $\mathbf{A}^T \mathbf{A} = \mathbf{I}$ .

**Remark 3.1** The spectral low-rank projection step has no influence on the spatial structure of  $\mathcal{Y}$ . This can be verified as follows: given two cubes  $\mathcal{Y}_i$  and  $\mathcal{Y}_j$  of the same size,  $\|\mathcal{Y}_i \times_3 \mathbf{A} - \mathcal{Y}_j \times_3 \mathbf{A}\|_F^2 = \|\mathcal{Y}_i - \mathcal{Y}_j\|_F^2 = \|\mathcal{Y}_i\|_F^2 + \|\mathcal{Y}_j\|_F^2 - 2\langle \mathcal{Y}_i, \mathcal{Y}_j \rangle$ .



**Spatial sparsity:** Based on **Remark 3.1**,  $\mathcal{G}$  should share the spatial structure with  $\mathcal{Y}$ . In this paper, we resort to use sparse and redundant representation to model the local 3D cubes within  $\mathcal{G}$ . This can be implemented by dividing  $\mathcal{G}$  into a number of small fully overlapping cubes, calculating their sparsity, and putting back to the original position using their denoised estimation by averaging with their overlapped cubes. 1D vector based sparse representation inevitably breaks local structure of MD signals and increases the demand of memory and computational cost [37]. To this end, we instead leverage tensor based multidimensional sparse representation framework. Let  $\mathcal{R}_i$  denote an operator extracting the  $i$ -th cube from  $\mathcal{G}$ , then each cube  $\mathcal{R}_i\mathcal{G}$  can be represented by

$$\mathcal{R}_i\mathcal{G} = \mathcal{B}_i \times_1 \mathbf{D}_1 \times_2 \mathbf{D}_2 \times_3 \mathbf{D}_3, \|\mathcal{B}_i\|_0 \leq K \quad (3)$$

where  $\mathbf{D}_i \in \mathbb{R}^{I_i \times M_i}$  ( $i = 1, 2, 3$ ) is the overcompleted dictionary matrix along  $i$ -th mode with  $I_i \leq M_i$  and  $\|\mathcal{B}_i\|_0$  is a tensor with less than  $K$  non-zeros.

Substituting Eq. (2) and Eq. (3) into Eq. (1), the proposed subspace based MD sparse representation denoising method is written as

$$\begin{aligned} \{\mathbf{A}^*, \mathcal{G}, \mathcal{B}_i^*\} = \arg \min_{\mathbf{A}, \mathcal{G}, \mathcal{B}_i} & \frac{1}{2} \|\mathcal{G} \times_3 \mathbf{A} - \mathcal{Y}\|_F^2 \\ & + \mu \sum_i \frac{1}{2} \|\mathcal{R}_i\mathcal{G} - \mathcal{B}_i \times_1 \mathbf{D}_1 \times_2 \mathbf{D}_2 \times_3 \mathbf{D}_3\|_F^2 + \lambda \|\mathcal{B}_i\|_0 \\ \text{s.t. } & \mathbf{A}^T \mathbf{A} = \mathbf{I} \end{aligned} \quad (4)$$

where  $\mathbf{D}_i$  is assumed to be pre-specified for example DCT dictionary or learned dictionary. In Eq. (4), the first term is data fidelity that demands a proximity between the observed noisy  $\mathcal{Y}$  and estimated image  $\mathcal{G} \times_3 \mathbf{A}$ . The second term stands for the prior assumption on  $\mathcal{G}$  that every cube  $\mathcal{R}_i\mathcal{G}$  has an MD sparse representation and  $\lambda > 0$  control the level of sparse regularization.  $\mu$  balances the data fidelity and sparse representation and can be implicitly set to 1.

### C. Model Optimization

Eq. (4) is difficult to solve because of complicated constraint on  $\mathbf{A}$  and  $\mathcal{B}_i$ . Similar to [14], [49], we solve Eq. (4) in a greedy way, which includes learning of the subspace  $\mathbf{A}$  from  $\mathcal{Y}$  and MD sparse representation  $\mathcal{B}_i^*$  from  $\mathcal{G}$ .

1) *Learning  $\mathbf{A}$ :* The optimization of  $\mathbf{A}$  can be considered as a Tucker-1 decomposition problem. Under the framework of higher-order singular value decomposition (HOSVD), we can obtain  $\mathbf{A}$  by performing singular decomposition on the unfolded matrix  $\mathbf{Y}_3$  along the spectral dimension, i.e.,  $\mathbf{Y}_3 = \mathbf{U}\mathbf{S}\mathbf{V}^T$ . Then,  $\mathbf{A}$  is assigned with  $\mathbf{A} = \mathbf{V}(1 : R, :)$  where  $R$  is estimated by the Hysime algorithm [50]. In order to more accurately estimate  $R$  and  $\mathbf{A}$ , some fast denoising methods such as NLM [32] and BM3D [33] can be applied. Once  $\mathbf{A}$  is obtained,  $\mathcal{G}$  can be obtained by

$$\mathcal{G} = \mathcal{Y} \times_3 \mathbf{A}^T \quad (5)$$

2) *Learning  $\mathcal{B}_i$ :* The  $L_0$  norm of  $\mathcal{B}$  is intractable because of its NP-hard property. It can be relaxed to the  $L_1$  norm to result in a convex optimization problem. Along this line, the optimization problem of  $\mathcal{B}_i$  can be formulated by

$$\arg \min_{\mathcal{B}_i} \frac{1}{2} \|\mathcal{R}_i\mathcal{G} - \mathcal{B}_i \times_1 \mathbf{D}_1 \times_2 \mathbf{D}_2 \times_3 \mathbf{D}_3\|_F^2 + \lambda \|\mathcal{B}_i\|_1 \quad (6)$$

This problem can be solved with Tensor-based Iterative shrinkage Thresholding Algorithm (TISTA) [37] with the following solution:

$$\begin{aligned} \mathcal{B}_i^{(k+1)} = & P_{\lambda/L}(\mathcal{B}_i^{(k)} - \frac{1}{L}(\mathcal{B}_i^{(k)} \times_1 \mathbf{D}_1^T \mathbf{D}_1 \times_2 \mathbf{D}_2^T \mathbf{D}_2 \times_3 \mathbf{D}_3^T \mathbf{D}_3 \\ & - \mathcal{R}_i\mathcal{G} \times_1 \mathbf{D}_1^T \times_2 \mathbf{D}_2^T \times_3 \mathbf{D}_3^T)) \end{aligned} \quad (7)$$

where  $L$  is a Lipschitz constant,  $P_{\lambda/L} = \text{sgn}(x)(|x| - \lambda)_+$  performs soft-thresholding operation to achieve the sparsity of  $\mathcal{B}_i^{(k+1)}$  and  $k$  indexes the iteration number.

After obtaining  $\mathcal{B}_i$ ,  $\hat{\mathcal{G}}$  can be obtained by averaging  $m$  estimates for each entry in the cube, i.e.,

$$\hat{\mathcal{G}} = \frac{1}{m} \sum_i \mathcal{R}_i' \mathcal{B}_i \times_1 \mathbf{D}_1 \times_2 \mathbf{D}_2 \times_3 \mathbf{D}_3 \quad (8)$$

where  $\mathcal{R}_i'$  is a linear operator placing back the cube  $\mathcal{B}_i \times_1 \mathbf{D}_1 \times_2 \mathbf{D}_2 \times_3 \mathbf{D}_3$  at the position centered on entry  $i$ . Finally, the output denoised HSI  $\hat{\mathcal{X}}$  can be obtained by Eq. (2). Algorithm 1 summarizes the denoising procedure of SMDS method.

---

#### Algorithm 1 SMDS for HSI denoising.

---

**Input:** Noisy HSI  $\mathcal{Y}$ , noise variance  $\sigma^2$ .

**Output:**  $\mathbf{A}$ ,  $\mathcal{G}$ , and  $\mathcal{X}$ .

- 1: Estimate  $R$  using Hysime [50].
  - 2: Conduct SVD on  $\mathbf{Y}_{(3)}$ , i.e.,  $\mathbf{Y}_{(3)} = \mathbf{U}\mathbf{S}\mathbf{V}^T$  and set  $\mathbf{A} = \mathbf{V}(1 : R, :)$ . *//subspace learning*
  - 3: Project  $\mathcal{Y}$  to obtain  $\mathcal{G}$  with Eq. (5). *//subspace projection*
  - 4: **repeat**
  - 5:   Compute  $\mathcal{B}_i$  with Eq. (7). *//MD sparse coding*
  - 6:   **until** TISTA converges.
  - 7: Obtain  $\hat{\mathcal{G}}$  with Eq. (8). *//cube aggregation*
  - 8: Output the estimated  $\mathcal{X}$  with Eq. (2). *//image reconstruction*
- 

## IV. UNFOLDED SMDS NETWORK

We unfold all the steps of SMDS as network layers to yield an end-to-end neural network for discriminative training. Deep unfolding starts from the iterative algorithm deduced by the model-based methods and maps each iteration into a typical layer of deep neural network. By stacking a predefined number of layers, a hierarchical deep network architecture can be obtained. Thanks to its merits of high interpretability, good generalization capability, strong learning ability and computational efficiency, deep unfolding networks have been successfully applied in many tasks, such as hyperspectral fusion [47], rain removal [51], image deblurring [52]. To this end, we unfold Algorithm 1 to obtain an end-to-end HSI denoising network.



### A. Network Architecture

Algorithm 1 can be decomposed into five stages. HSIs may have different bands and reside in different subspaces, making it difficult to be embedded as network parameter for discriminative learning. For this reason,  $\mathbf{A}$  is precomputed and taken as network input along with  $\mathcal{Y}$ . The output of the network is the denoised  $\hat{\mathcal{X}}$ . Moreover, the cube extraction step can be easily implemented with built-in function of existing deep learning framework. The other key stages are listed as follows:

**Subspace projection:** The first stage of the network is mapping  $\mathcal{Y}$  into a low-dimensional subspace held by  $\mathbf{A}$  following Eq. (5). This can be realized by a  $1 \times 1$  2D convolution whose weights are set as  $\mathbf{A}$ .

**MD sparse coding:** After cube extraction, MD sparse coding stage learns the sparse coding of each cube with respect to multidimensional dictionaries, corresponding to Eq. (7). Eq. (7) can be further decomposed into the following three steps:

$$\mathcal{E}_i^{(k+1)} = \mathcal{R}_i \mathcal{G} - \mathcal{B}_i^{(k)} \times_1 \mathbf{D}_1 \times_2 \mathbf{D}_2 \times_3 \mathbf{D}_3 \quad (9)$$

$$\mathcal{H}_i^{(k+1)} = \mathcal{B}_i^{(k)} + \mathcal{E}_i^{(k+1)} \times_1 \mathbf{C}_1^T \times_2 \mathbf{C}_2^T \times_3 \mathbf{C}_3^T \quad (10)$$

$$\mathcal{B}_i^{(k+1)} = P_{\Lambda^{(k+1)}}(\mathcal{H}_i^{(k+1)}) \quad (11)$$

where  $\Lambda^{(k+1)} \in \mathbb{R}^{M_1 \times M_2 \times M_3}$  denotes the thresholding parameter tensor for  $\mathcal{H}_i^{(k)}$  in the  $k$ -th layer of MD sparse coding module. Following [53], we decouple  $\mathbf{C}$  from  $\mathbf{D}$  and set different  $\Lambda$  in each layer for accelerated convergence.

Eq. (9) and Eq. (10) are similar in function, mapping the processed tensor to a new dimension along three modes. Eq. (9) can be realized by three  $1 \times 1$  2D convolutions with corresponding to  $\{\mathbf{D}_1, \mathbf{D}_2, \mathbf{D}_3\}$ . In the same way, Eq. (10) can be performed by  $1 \times 1$  transposed 2D convolutions along three modes of a tensor whose weights are related with  $\{\mathbf{C}_1, \mathbf{C}_2, \mathbf{C}_3\}$ .  $P_{\Lambda^{(k)}}$  in Eq. (11) corresponds to the nonlinear function allowing for the sparsity of  $\mathcal{H}^{(k)}$ , which can be implemented with  $\text{Relu}(x - \theta) - \text{Relu}(-x - \theta)$ . By stacking Eqs. (9), (10) and (11) for  $K$  times, we can now obtain a subnetwork for MD sparse coding, i.e., the highlighted part in Figure 2.

**Cube aggregation:** Similarly, Eq. (8) can also be interpreted as three linear transformation layers with an averaging layer. As in [54], [55], we decouple  $\mathbf{W}$  from  $\mathbf{D}$  for effective end-to-end training, i.e.,  $\hat{\mathcal{G}} = \frac{1}{m} \sum_{i=1}^n \mathcal{R}_i \mathcal{B}_i^{(K)} \times_1 \mathbf{W}_1 \times_2 \mathbf{W}_2 \times_3 \mathbf{W}_3$ , which can be implemented with transposed convolutions with kernel size of  $1 \times 1$  whose weight respectively corresponds to  $\{\mathbf{W}_1, \mathbf{W}_2, \mathbf{W}_3\}$ .

**Image reconstruction:** This stage produces the denoised HSIs  $\hat{\mathcal{X}}$  using Eq. (2), which can also be achieved by a  $1 \times 1$  transposed convolution with weights given by  $\mathbf{A}$ .

### B. Network Training

**Training loss:** The training loss for given training set of noisy-clean pairs is defined as the Euclidean distance between the output of SMDS-Net and the ground truth  $\mathcal{X}$ , i.e.,

$$L = \|\text{SMDS-Net}(\mathcal{Y}, \Theta) - \mathcal{X}\|_F^2 \quad (12)$$

where  $\Theta = \{(\mathbf{C}_j, \mathbf{D}_j, \mathbf{W}_j)_{j=1,2,3}, (\Lambda^{(k)})_{k=1,\dots,K}\}$  represents all parameters to be learned.

**Implement details:** SMDS-Net is implemented on the Pytorch platform and trained on three NVIDIA Titan V GPUs with 300 epochs. We adopt the Adam optimizer with the batch size of 3 and patch size of  $56 \times 56$ . The initial learning rate is  $10^{-3}$  and multiplied by 0.35 for every 80 epochs. The cube size  $[I_1, I_2, I_3]$  is set as  $[5, 5, 5]$ . The number of dictionaries  $[M_1, M_2, M_3]$  are given by  $[9, 9, 9]$ , leading to dictionaries size of  $5 \times 9$  along three modes. The number of unfolding  $K$  is set to 24. Detailed analysis of these parameters are provided in supplementary material.

**Training dataset:** Our training dataset contains 33 pairs of HSIs including two subsets: close-range HSIs and remote sensing HSIs. The HSIs in close-range parts are randomly selected from CAVE Dataset<sup>1</sup> with 31 bands. images in the remote sensing subset are constructed by Reno with 356 bands<sup>2</sup>, San Diego Airport with 189 bands<sup>3</sup>, HYDICE Washington DC Mall dataset with 191 bands<sup>4</sup> and Apex open source data cube<sup>5</sup> with 285 bands. Data augmentation is performed including random flipping, cropping and resizing.

## V. EXPERIMENTAL RESULTS

### A. Evaluation Measures

Both quantitative and qualitative results are provided to thoroughly evaluate the denoising ability of all the methods. Besides three conventional picture quality indices (PQIs), PSNR, SSIM and FSIM, we also adopt erreur relative globale adimensionnelle de synthese (ERGAS) and spectral angle mapper (SAM) for quantitative assessment. ERGAS records the fidelity of the recovered image by computing the weighted sum of mean squared error (MSE). SAM provides the spectral differences between reference HSI and the denoised HSI. Smaller ERGAS and SAM and larger PSNR, SSIM and FSIM imply better denoising results. We compare the restored HSI with the clean HSI to illustrate their differences for qualitative analysis.

### B. Methods of Comparison

The competing denosing methods include: four sparse representation based methods, i.e., BM3D [33]<sup>6</sup>, BM4D [34]<sup>7</sup>, TDL [20]<sup>8</sup>, MTSNMF [1], five low-rank representation based methods, i.e., LRTA [18]<sup>9</sup>, PARAFAC [19], FastHyDe [49]<sup>10</sup>, KBR [2]<sup>11</sup>, NGMeet [14]<sup>12</sup> and three deep learning based

<sup>1</sup><https://www.cs.columbia.edu/CAVE/databases/multispectral/>

<sup>2</sup><https://www.spectir.com/contact#free-data-samples>

<sup>3</sup><https://github.com/ShoupingShan/Hyperspectral-image-target-detection-based-on-sparse-representation>

<sup>4</sup><https://rslab.ut.ac.ir/data>

<sup>5</sup><https://apex-esd.org/en/data/free-data-cubes>

<sup>6</sup><http://www.cs.tut.fi/foi/GCF-BM3D>

<sup>7</sup><http://www.cs.tut.fi/foi/>

<sup>8</sup><http://gr.xjtu.edu.cn/web/dymeng/>

<sup>9</sup><https://www.sandia.gov/tgkolda/TensorToolbox/>

<sup>10</sup><http://www.lx.it.pt/~bioucas/>

<sup>11</sup><http://gr.xjtu.edu.cn/web/dymeng/>

<sup>12</sup>[github.com/quanmingyao/NGMeet](https://github.com/quanmingyao/NGMeet)

TABLE I  
COMPARISON OF DIFFERENT METHODS ON CAVE AND ICVL IMAGE

Image	$\sigma$	Index	Noisy	Sparse methods				Low-rank methods					DL methods			
				BM3D [33]	BM4D [34]	TDL [20]	MTSNMF [1]	LRTA [18]	PARAFAC [19]	FastHyDe [49]	KBR [2]	NGMeet [14]	Dn-CNN [3]	HSI-SDeCNN [22]	HSID-CNN [25]	SMDS-Net
CAVE	[0-15]	PSNR	31.6	37.21	43.39	33.79	42.31	36.02	30.59	38.67	43.89	37.09	32.73	40.18	36.56	<b>44.66</b>
		SSIM	0.5797	0.9632	0.7300	0.9713	0.9742	0.8382	0.8339	0.9623	0.9752	0.8515	0.8372	0.9748	0.9570	<b>0.9857</b>
		FSIM	0.9089	0.9837	0.9915	0.9516	0.9912	0.9553	0.9131	0.9896	0.9946	0.9720	0.9402	0.9886	0.9779	<b>0.9952</b>
		ERGAS	159.4	56.17	36.27	115.4	31.48	75.31	119.2	60.28	27.73	83.75	93.76	60.20	72.09	<b>25.06</b>
		SAM	0.7333	0.1373	0.1799	0.5969	0.1345	0.4465	0.3272	0.2379	0.2042	0.5064	0.2074	0.1949	0.2399	<b>0.1097</b>
	[0-55]	PSNR	22.66	32.75	38.10	27.87	35.63	27.92	30.19	34.83	35.04	30.12	32.13	35.24	33.74	<b>38.93</b>
		SSIM	0.3026	0.8046	<b>0.9456</b>	0.4998	0.8823	0.5122	0.8092	0.9237	0.7949	0.7009	0.8167	0.8760	0.9029	0.9363
		FSIM	0.7302	0.9270	0.9784	0.8595	0.9579	0.8365	0.9026	0.9729	0.9534	0.9031	0.9291	<b>0.9841</b>	0.9550	0.9804
		ERGAS	444.8	163.6	54.06	258.8	114.5	220.4	124.8	84.93	108.1	251.0	111.7	82.42	124.5	<b>46.92</b>
		SAM	1.003	0.5429	0.2486	0.8613	0.3999	0.8154	0.3344	0.3261	0.6405	0.8639	0.3029	0.2744	0.3226	<b>0.2717</b>
	[0-95]	PSNR	19.01	26.32	34.25	23.42	31.75	23.56	29.43	29.53	32.33	25.07	26.81	31.69	30.89	<b>36.00</b>
		SSIM	0.2280	0.5475	0.8549	0.3619	0.8003	0.3565	0.7449	0.8895	0.7708	0.5105	0.5781	0.7546	0.8650	<b>0.8982</b>
		FSIM	0.6207	0.7850	0.9505	0.7453	0.9120	0.7303	0.8855	0.9497	0.9296	0.8193	0.7924	0.9284	0.9425	<b>0.9612</b>
		ERGAS	807.8	480.2	92.22	495.6	208.9	419.8	136.3	143.4	138.2	485.5	376.0	116.4	195.4	<b>66.11</b>
		SAM	1.131	0.8180	0.4745	1.014	0.5533	0.9796	0.4526	0.3817	0.6449	1.034	0.8223	<b>0.3241</b>	0.3801	0.3401
ICVL	[0-17]	PSNR	31.87	38.57	42.65	37.53	44.18	37.40	32.06	44.32	44.12	39.16	32.48	40.57	37.10	<b>45.00</b>
		SSIM	0.6598	0.9515	0.9800	0.8680	0.9615	0.8791	0.8742	<b>0.9895</b>	0.9820	0.8822	0.8571	0.9556	0.9652	0.9863
		FSIM	0.9492	0.9690	0.9901	0.9813	0.9902	0.9674	0.9182	0.9931	0.9924	0.9792	0.8816	0.9898	0.9711	<b>0.9932</b>
		ERGAS	125.9	40.57	24.59	63.16	34.89	58.75	85.59	21.40	21.80	67.68	82.60	35.72	64.04	<b>19.68</b>
		SAM	0.1621	0.0266	0.0301	0.0784	0.0356	0.0731	0.0504	0.0211	0.0225	0.0831	0.0345	0.0345	0.0595	<b>0.0180</b>
	[0-55]	PSNR	22.37	32.18	37.03	27.85	37.25	27.86	31.83	38.54	34.55	30.14	31.53	34.72	32.58	<b>39.14</b>
		SSIM	0.3129	0.7331	0.9138	0.5287	0.8740	0.5423	0.8589	<b>0.9675</b>	0.8040	0.7156	0.8016	0.8416	0.8920	0.9619
		FSIM	0.8075	0.9049	0.9623	0.8989	0.9613	0.8747	0.9156	<b>0.9814</b>	0.9562	0.9142	0.8806	0.8416	0.9341	0.9777
		ERGAS	399.0	189.3	61.18	229.5	115.3	210.1	88.14	51.77	98.72	251.4	111.2	76.74	130.2	<b>38.74</b>
		SAM	0.4586	0.2211	0.0598	0.2746	0.1242	0.2528	0.0514	0.0505	0.1161	0.2858	0.1020	0.0677	0.0990	<b>0.0358</b>
	[0-95]	PSNR	16.49	23.52	33.79	24.41	33.19	24.63	30.43	32.60	33.97	26.52	24.66	29.85	29.79	<b>36.15</b>
		SSIM	0.1574	0.4145	0.8724	0.3980	0.8077	0.4069	0.7861	<b>0.9388</b>	0.8722	0.5961	0.4855	0.6849	0.8774	<b>0.9315</b>
		FSIM	0.6747	0.7679	0.9351	0.8414	0.9344	0.8095	0.9026	0.9571	0.9531	0.8751	0.7745	0.9187	0.9229	<b>0.9636</b>
		ERGAS	730.5	494.3	76.79	319.3	186.3	288.7	104.1	87.78	73.86	397.7	382.6	120.7	252.2	<b>52.79</b>
		SAM	0.7275	0.5261	0.0778	0.3834	0.2031	0.3462	0.0687	0.0909	0.0730	0.4418	0.4349	0.1053	0.1544	<b>0.0415</b>

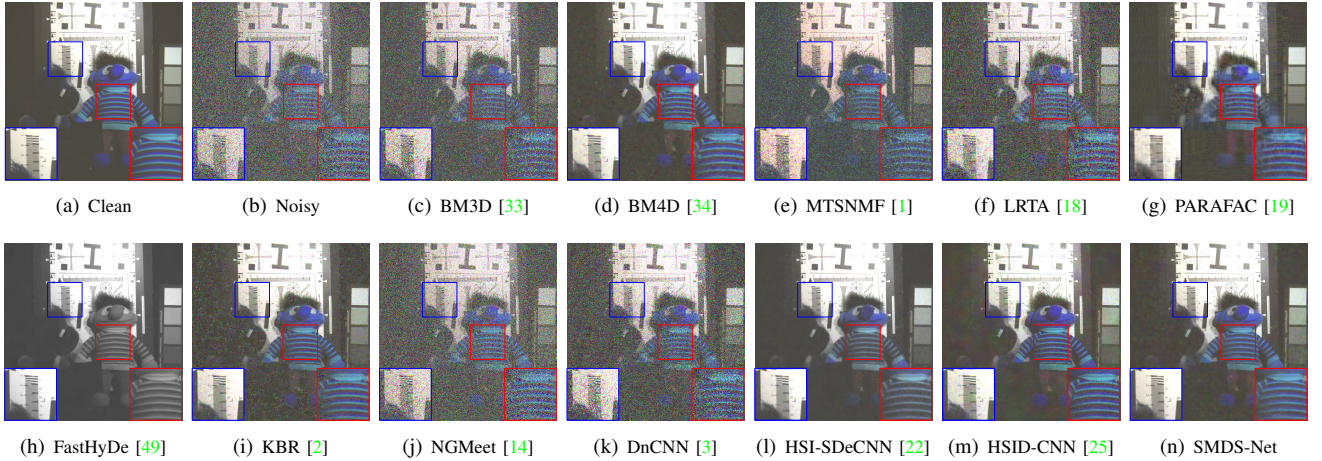


Fig. 3. Denoising results on the CAVE chart and stuffed toy image with the noise variance [0-95]. The false-color images were generated by combining bands 9, 15, 28. SMDS-Net achieves the best visual results with less artifacts.

methods, i.e., DnCNN [3]<sup>13</sup>, HSI-SDeCNN [22]<sup>14</sup> and HSID-CNN [25]<sup>15</sup>. HSI-SDeCNN and HSID-CNN are developed

<sup>13</sup><https://github.com/csxn/DnCNN>

<sup>14</sup><https://github.com/mhaut/HSI-SDeCNN>

<sup>15</sup><https://github.com/qzhang95/HSID-CNN>



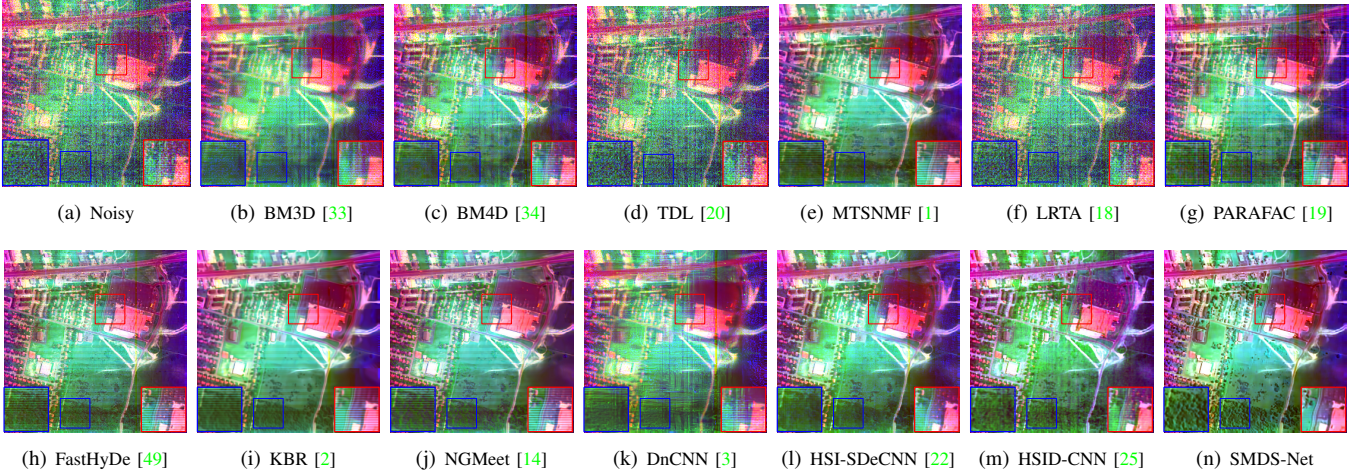


Fig. 4. Denoising results on real remote sensing Urban dataset. The false-color images were generated by combining bands 1, 108, and 208. The proposed SMDS-Net produces the most appealing visual results.

specifically for HSI. BM3D and DnCNN are performed in band by band manner. The parameters and networks of compared algorithms are optimally set or automatically chosen as described in the original references. We are especially interested in MTSNMF, KBR, NGMeet Dn-CNN, HSI-SDeCNN and HSID-CNN, as they are more related to the proposed SMDS-Net.

### C. Experiments with Synthetic Data

The synthetic data are generated by manually adding different standard deviations ( $\sigma$ ) of additive white Gaussian noise (AWGN) to each band of clean HSI. Specifically  $\sigma$  is chosen in three ranges, i.e., [0-15], [0-55] and [0-95].

1) *Quantitative Comparison:* We select CAVE *chart* and *stuffed toy* and a subscene of ICVL *BGU campus*<sup>16</sup> image for experiment, respectively shown in Figure 5 and Figure 1. Both of them are size of  $512 \times 512 \times 31$ . The denoising results are shown in Table I, in which the best results are highlighted in bold. As can be seen, the proposed SMDS-Net achieves state-of-the-art results by providing the best denoising performance in most cases. This is owing to the hybrid advantages of low-rank multidimensional sparse model and learning ability of DL. MTSNMF performs well when  $\sigma < 55$  but poorly in heavily noisy cases. The main reason is that it only considers the spatial sparse coding of all the bands but fails to consider the correlation between dictionaries. NGMeet loses its effectiveness, specially in very noisy cases. The main reason is that, the noise variances of all the bands are different, violating the claimed assumption that the noise variances remain unchanged in low-dimensional subspace and subspace adjustment of NGMeet. This phenomenon also implies the drawbacks of traditional model-based methods in troublesome parameter tuning and precisely modeling. Moreover, band-wise DnCNN also provides unsatisfactory performance because of the ignorance of prior knowledge of HSIs.

2) *Visual Comparison:* To thoroughly present the denoising effectiveness of our method, we present the visual denoising

results of all the methods on *chart* and *stuffed toy* image in Figure 5, where the false-color images are generated by using bands 9, 15, 28. Generally, tensor based methods provide more appealing visual results thanks to better consideration of the spectral-spatial structure of HSIs. The color style of FastHyDe are very different from the reference one because of inaccurate estimation of the spectral subspace. From highlighted areas, we can see KBR, MTSNMF and DnCNN can not remove all the noises and DnCNN produces very blur results, which however is not the case for SMDS-Net. Thanks to the strong physical model considering the spatial and spectral properties of HSIs and learning ability of unfolded network, SMDS-Net is able to produce the best visual quality.

### D. Experiments with Real Data.

We run all the competing methods on widely used Urban dataset. Different from HSIs in CAVE and ICVL captured in close-range scenarios, Urban dataset is a remote sensing HSI with much lower spatial resolution but higher spectral resolution. This dataset contains heavy noises, especially in bands 1, 105, 108, 207, 208. By compositing bands 1,108,208 as false-color images, Figure 4 shows the denoising results. As can be clearly seen, our method obtains the best denoising results.

## VI. CONCLUSION

In this paper, we introduce a model guided deep neural network, i.e., SMDS-Net for HSI denoising. Experimental results show that MDS-Net provides the state-of-the-art denoising performance with higher interpretability, implying the benefits of equipping DL with model priors. In future, we will integrate the nonlocal similarity prior of HSIs into the network for more powerful denoising ability.

## APPENDIX A EXPERIMENTS ON REMOTE SENSING HSI

Here, we present the quantitative denoising results of all the competing methods on remote sensing HSI in terms of PSNR,

<sup>16</sup><http://icvl.cs.bgu.ac.il/hyperspectral/>



TABLE II  
COMPARISON OF DIFFERENT METHODS ON PAVIA CENTER HSI.

			Sparse methods				Low-rank methods					DL methods			
$\sigma$	Index	Noisy	BM3D [33]	BM4D [34]	TDL [20]	MTSNMF [1]	LRTA [18]	PARAFAC [19]	FastHyDe [49]	KBR [2]	NGMeet [14]	Dn-CNN [3]	HSI-SDeCNN [22]	HSID-CNN [25]	SMDS-Net
[0-95]	PSNR	16.90	20.24	29.12	23.02	31.20	22.18	27.72	32.18	30.26	27.57	26.33	30.14	29.67	<b>32.73</b>
	SSIM	0.3176	0.4345	0.8243	0.5560	0.8918	0.5139	0.7897	0.9222	0.8717	0.7862	0.6746	0.8665	0.8499	<b>0.9290</b>
	FSIM	0.6112	0.7039	0.8885	0.7803	0.9411	0.7396	0.8731	0.9484	0.9200	0.8824	0.8112	0.9287	0.8993	<b>0.9523</b>
	ERGAS	787.6	540.8	129.9	347.8	107.2	354.1	162.6	94.98	115.3	276.6	3204	119.1	119.9	<b>85.03</b>
	SAM	0.8551	0.6257	0.1826	0.5078	0.1252	0.5094	0.2600	0.1237	0.1410	0.4431	0.2546	0.1640	0.1167	<b>0.1069</b>

TABLE III  
THE INFLUENCE OF THE NUMBER OF UNFOLDING  $K$ .

$K$	3	6	9	12	15	18	21	24	27	30
PSNR	37.74	37.77	37.83	37.81	<b>37.89</b>	37.76	37.79	37.75	37.75	37.74
SSIM	0.9520	0.9511	0.9533	<b>0.9556</b>	0.9553	0.9549	0.9543	0.9520	0.9536	0.9511
FSIM	0.9759	0.9761	0.9768	0.9768	0.9773	0.9771	<b>0.9766</b>	0.9764	0.9770	0.9761
ERGAS	50.36	50.18	49.73	49.83	<b>49.28</b>	49.97	49.92	50.13	50.01	50.34
SAM	0.1389	0.1441	0.1347	<b>0.1247</b>	0.1290	0.1282	0.1317	0.1358	0.1304	0.1403
#Parameters	<b>2592</b>	4779	6966	9153	11340	13527	15714	17901	20088	22275

SSIM, FSIM, ERGAS and SAM. A subscene of Pavia Center HSI containing  $200 \times 200$  pixels and 80 bands is used for experiment. Setting noise standard variance  $\sigma$  in the range of 0 to 90, Table II shows the denoising accuracy of all the methods. Generally, spectral-spatial methods have higher denoising capability, for example, BM3D versus BM4D, Dn-CNN versus HSI-SDeCNN. Compared with alternative DL methods, the proposed SMDS-Net provides considerably better performance thanks to hybrid advantages of powerful denoising model and learning ability of DL.

## APPENDIX B NETWORK ANALYSIS

In general, the number of unfolding ( $K$ ), the dictionary number ( $[M_1, M_2, M_3]$ ) and the cube size ( $[I_1, I_2, I_3]$ ) are three factors influencing the denoising effectiveness of SMDS-Net. In this section, we conduct a comprehensive study on these key parameters. We add additive white Gaussian noise (AWGN) to every band whose stand deviation  $\sigma$  is set between 0 and 55 to CAVE chart and stuffed toy, ICVL BGU, and Pavia Center HSIs. The averaged denoising performance on three HSIs is reported.

### A. Study of Unfolded Iteration $K$

$K$  indexes the number of unfolding and also directly controls the depth of the network. Table III presents the denoising result with respect to  $K$  setting. SMDS-Net takes the advantages of back propagation and forward propagation to establish the relationship between current iteration and historical iterations which enforces the network to simultaneously takes historical information and current information into consideration for parameter update. This leads to the phenomenon that  $K$  has insignificant influence on denoising performance as shown in Table III, implying layer number of SMDS-Net is easy to choose. Moreover, even setting  $K = 30$ , the

number of parameters is 22275 and noticeably less than that of HSI-SDeCNN [22], i.e., over 1 million. This attributes to the adoption of spectral low-rank projection and multidimensional sparse coding. The small number of parameters also reduces the requirement of training samples size. As we can obtain slightly better denoising accuracy when  $K = 15$ , we set  $K$  to 15 in the following network analysis.

### B. Study of Denoising Behavior of Each Layer

As mentioned earlier, SMDS-Net includes five stages: subspace projection, cube extraction, multidimensional sparse coding (MDS), cube aggregation and image reconstruction. From the optimization of MDS, i.e., tensor-based iterative shrinkage thresholding algorithm, theoretically, each layer of MDS sparsely encodes an input data cube and gradually filters out the noises. After the model is trained under the setting of  $K = 15$ , we also change the number of unfolded iterations to see whether MDS has denoising ability as expected. This is implemented by multiplying the multidimensional sparse coding in the  $k$ -th ( $0 < k \leq 15$ ) unfolded layer with dictionary  $\{\mathbf{W}_1, \mathbf{W}_2, \mathbf{W}_3\}$  to reconstruct the cube at test time. All the other steps are kept the same. As shown in Figure 5, the denoising performance firstly degrades in the first few layers ( $0 < k \leq 9$ ) possibly because the network is trying to adapt to the data. Afterwards, the denoising performance gradually reaches better results, by presenting more appealing visual appearance and higher PSNR value. The results in Figure 5 suggest that all the layers progressively learn to obtain a better sparse estimation as the theory indicated, implying its interpretability, which facilitates generalizing to unseen samples.

### C. Study of Dictionary Number

We measure the influence of the dictionary number in Table IV. For simplicity, we set  $M_1 = M_2 = M_3$  and choose

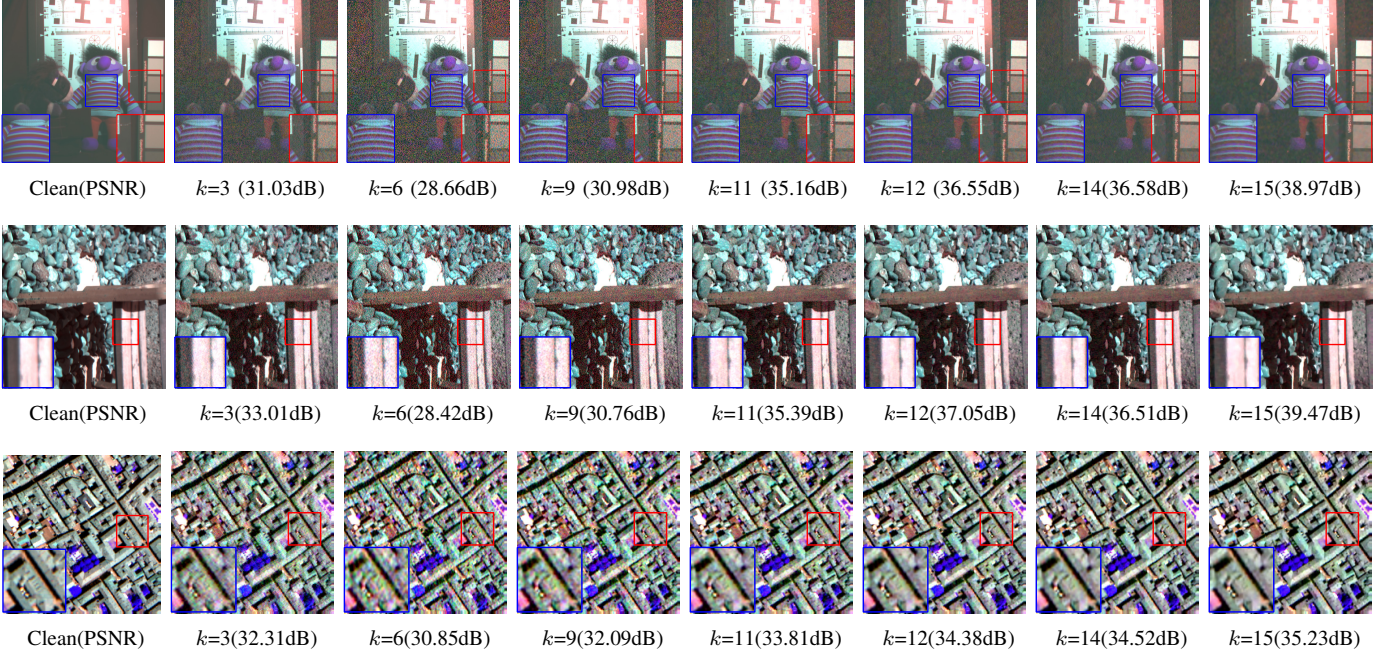


Fig. 5. The denoising behavior of each layer of SMDS-Net when  $K = 15$ .

the value from the set of  $\{5, 7, 9, 11, 13\}$ . As shown in the table, setting the dictionary number as  $[9, 9, 9]$  allows for the most favorable denoising accuracy. Therefore, the dictionary number is suggested to set as  $[9, 9, 9]$ .

TABLE IV  
THE INFLUENCE OF THE DICTIONARY NUMBER.

$[M_1, M_2, M_3]$	$[5, 5, 5]$	$[7, 7, 7]$	$[9, 9, 9]$	$[11, 11, 11]$	$[13, 13, 13]$
PSNR	37.59	37.79	<b>37.89</b>	37.70	37.84
SSIM	0.9482	0.9506	<b>0.9553</b>	0.9529	0.9546
FSIM	0.9748	0.9759	<b>0.9773</b>	0.9766	0.9772
ERGAS	51.41	50.11	<b>49.29</b>	50.42	49.58
SAM	0.1532	0.1449	0.1290	0.1350	<b>0.1284</b>
#Parameters	2100	5460	11340	20460	33540

TABLE V  
THE INFLUENCE OF CUBE SIZE.

$[I_1, I_2, I_3]$	$[3, 3, 3]$	$[5, 5, 5]$	$[7, 7, 7]$	$[9, 9, 9]$	$[11, 11, 11]$
PSNR	36.4302	<b>37.89</b>	36.98	37.15	37.47
SSIM	0.9340	0.9553	0.9529	0.9575	<b>0.9604</b>
FSIM	0.9672	<b>0.9773</b>	0.9737	0.9744	0.9762
ERGAS	59.01	<b>49.29</b>	54.48	53.17	51.05
SAM	0.1656	0.1290	0.1096	0.0946	<b>0.0942</b>
#Parameters	11178	11340	11502	11664	11826

#### D. Study of Cube Size

Last, we analyze the influence of cube size  $[I_1, I_2, I_3]$  on HSI denoising. As the experiment in the study of dictionary number,  $I_1, I_2$  and  $I_3$  are set the same. By changing the size from 3 to 11 with an interval of 2, Table V presents the

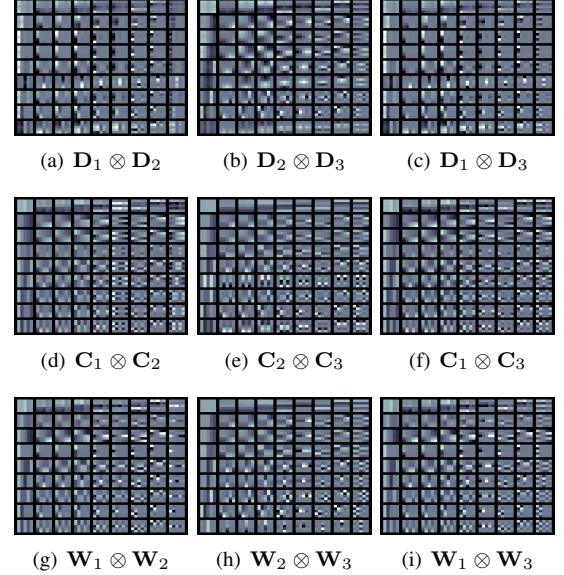


Fig. 6. Visualization of learned dictionaries for SMDS-Net when  $\{D_i, C_i, W_i\}_{i=1,2,3} \in \mathbb{R}^{5 \times 9}$ .

denoising ability of SMDS-Net. The denoising performance first becomes better when  $I_i$  ( $i=1,2,3$ ) increases from 3 to 5 and then drops a little when  $I_i > 5$ . From this experiment, it is recommended that the cube size is set as  $[5, 5, 5]$ , balancing the denoising performance and the number of parameters.

#### E. Visualization of Learned Dictionaries.

Setting the cube size as  $5 \times 5 \times 5$  and dictionary number along each mode as  $[9, 9, 9]$ , Figure 6 visualizes the learned dictionaries which are constructed by the Kronecker product of  $D, W$  and  $C$  along arbitrary dimensions. As can be seen, the learned dictionary can capture the structure features in all the dimensions.

## REFERENCES

- [1] M. Ye, Y. Qian, and J. Zhou, "Multitask sparse nonnegative matrix factorization for joint spectral-spatial hyperspectral imagery denoising," *IEEE Trans. Geosci. Remote Sens.*, vol. 53, no. 5, pp. 2621–2639, 2015. [1, 2, 5, 6, 7, 8](#)
- [2] Q. Xie, Q. Zhao, D. Meng, and Z. Xu, "Kronecker-basis-representation based tensor sparsity and its applications to tensor recovery," *IEEE Trans. Pattern Anal. Mach. Intell.*, vol. 40, no. 8, pp. 1888–1902, 2018. [1, 2, 5, 6, 7, 8](#)
- [3] K. Zhang, W. Zuo, Y. Chen, D. Meng, and L. Zhang, "Beyond a gaussian denoiser: Residual learning of deep cnn for image denoising," *IEEE Trans. Image Process.*, vol. 26, no. 7, pp. 3142–3155, 2017. [1, 6, 7, 8](#)
- [4] C. Li, D. Song, R. Tong, and M. Tang, "Illumination-aware faster r-cnn for robust multispectral pedestrian detection," *Pattern Recognit.*, vol. 85, pp. 161–171, 2019. [1](#)
- [5] L. Zhang, X. Zhu, X. Chen, X. Yang, Z. Lei, and Z. Liu, "Weakly aligned cross-modal learning for multispectral pedestrian detection," in *In Proc. IEEE Int. Conf. Comput. Vis. (ICCV)*, 2019, pp. 5126–5136. [1](#)
- [6] D. Guan, X. Luo, Y. Cao, J. Yang, Y. Cao, G. Vosselman, and M. Y. Ying, "Unsupervised domain adaptation for multispectral pedestrian detection," in *Proc. IEEE Conf. Comput. Vis. Pattern Recognit. (CVPR) Workshops*, June 2019. [1](#)
- [7] F. Xiong, J. Zhou, and Y. Qian, "Material based object tracking in hyperspectral videos," *IEEE Trans. Image Process.*, vol. 29, pp. 3719–3733, 2020. [1](#)
- [8] Y. Zhou, H. Chang, K. Barner, P. Spellman, and B. Parvin, "Classification of histology sections via multispectral convolutional sparse coding," in *Proc. IEEE Conf. Comput. Vis. Pattern Recognit. (CVPR)*, 2014, pp. 3081–3088. [1](#)
- [9] W. He, H. Zhang, L. Zhang, and H. Shen, "Total-variation-regularized low-rank matrix factorization for hyperspectral image restoration," *IEEE Trans. Geosci. Remote Sens.*, vol. 54, no. 1, pp. 178–188, 2016. [1, 2](#)
- [10] Y. Fu, A. Lam, I. Sato, and Y. Sato, "Adaptive spatial-spectral dictionary learning for hyperspectral image denoising," in *In Proc. IEEE Int. Conf. Comput. Vis. (ICCV)*, 2015, pp. 343–351. [1, 2](#)
- [11] W. Wei, L. Zhang, C. Tian, A. Plaza, and Y. Zhang, "Structured sparse coding-based hyperspectral imagery denoising with intracluster filtering," *IEEE Trans. Geosci. Remote Sens.*, vol. 55, no. 12, pp. 6860–6876, 2017. [1, 2](#)
- [12] T. Lu, S. Li, L. Fang, Y. Ma, and J. A. Benediktsson, "Spectral-spatial adaptive sparse representation for hyperspectral image denoising," *IEEE Trans. Geosci. Remote Sens.*, vol. 54, no. 1, pp. 373–385, 2016. [1, 2](#)
- [13] J. Li, Q. Yuan, H. Shen, and L. Zhang, "Noise removal from hyperspectral image with joint spectral-spatial distributed sparse representation," *IEEE Trans. Geosci. Remote Sens.*, vol. 54, no. 9, pp. 5425–5439, 2016. [1](#)
- [14] W. He, Q. Yao, C. Li, N. Yokoya, and Q. Zhao, "Non-local meets global: An integrated paradigm for hyperspectral denoising," in *Proc. IEEE Conf. Comput. Vis. Pattern Recognit. (CVPR)*, 2019, pp. 6861–6870. [1, 2, 3, 4, 5, 6, 7, 8](#)
- [15] H. Zhang, W. He, L. Zhang, H. Shen, and Q. Yuan, "Hyperspectral image restoration using low-rank matrix recovery," *IEEE Trans. Geosci. Remote Sens.*, vol. 52, no. 8, pp. 4729–4743, 2014. [1](#)
- [16] Y. Chen, W. He, N. Yokoya, T. Huang, and X. Zhao, "Nonlocal tensoring decomposition for hyperspectral image denoising," *IEEE Trans. Geosci. Remote Sens.*, vol. 58, no. 2, pp. 1348–1362, 2020. [1, 2](#)
- [17] N. Qi, Y. Shi, X. Sun, J. Wang, B. Yin, and J. Gao, "Multi-dimensional sparse models," *IEEE Trans. Pattern Anal. Mach. Intell.*, vol. 40, no. 1, pp. 163–178, 2018. [1](#)
- [18] N. Renard, S. Bourennane, and J. Blanc-Talon, "Denoising and dimensionality reduction using multilinear tools for hyperspectral images," *IEEE Geosci. Remote Sens. Lett.*, vol. 5, no. 2, pp. 138–142, 2008. [1, 5, 6, 7, 8](#)
- [19] X. Liu, S. Bourennane, and C. Fossati, "Denoising of hyperspectral images using the parafac model and statistical performance analysis," *IEEE Trans. Geosci. Remote Sens.*, vol. 50, no. 10, pp. 3717–3724, 2012. [1, 5, 6, 7, 8](#)
- [20] Y. Peng, D. Meng, Z. Xu, C. Gao, Y. Yang, and B. Zhang, "Decomposable nonlocal tensor dictionary learning for multispectral image denoising," in *Proc. IEEE Conf. Comput. Vis. Pattern Recognit. (CVPR)*, 2014, pp. 2949–2956. [1, 2, 5, 6, 7, 8](#)
- [21] Y. Chang, L. Yan, and S. Zhong, "Hyper-laplacian regularized unidirectional low-rank tensor recovery for multispectral image denoising," in *Proc. IEEE Conf. Comput. Vis. Pattern Recognit. (CVPR)*, July 2017. [1, 2](#)
- [22] A. Maffei, J. M. Haut, M. E. Paoletti, J. Plaza, L. Bruzzone, and A. Plaza, "A single model cnn for hyperspectral image denoising," *IEEE Trans. Geosci. Remote Sens.*, vol. 58, no. 4, pp. 2516–2529, 2020. [1, 2, 6, 7, 8](#)
- [23] B. Lin, X. Tao, and J. Lu, "Hyperspectral image denoising via matrix factorization and deep prior regularization," *IEEE Trans. Image Process.*, vol. 29, pp. 565–578, 2020. [1, 2, 3](#)
- [24] Y. Chang, L. Yan, H. Fang, S. Zhong, and W. Liao, "Hsi-denet: Hyperspectral image restoration via convolutional neural network," *IEEE Trans. Geosci. Remote Sens.*, vol. 57, no. 2, pp. 667–682, 2019. [1, 2](#)
- [25] Q. Yuan, Q. Zhang, J. Li, H. Shen, and L. Zhang, "Hyperspectral image denoising employing a spatial-spectral deep residual convolutional neural network," *IEEE Trans. Geosci. Remote Sens.*, vol. 57, no. 2, pp. 1205–1218, 2019. [1, 2, 6, 7, 8](#)
- [26] W. Dong, H. Wang, F. Wu, G. Shi, and X. Li, "Deep spatial-spectral representation learning for hyperspectral image denoising," *IEEE Transactions on Computational Imaging*, vol. 5, no. 4, pp. 635–648, 2019. [1, 2](#)
- [27] Y. Zhao, D. Zhai, J. Jiang, and X. Liu, "Adm: Attention-based deep residual network for hyperspectral image denoising," in *Proc. IEEE International Conference on Acoustics, Speech and Signal Processing (ICASSP)*, 2020, pp. 2668–2672. [1, 2](#)
- [28] K. Wei, Y. Fu, and H. Huang, "3-d quasi-recurrent neural network for hyperspectral image denoising," *IEEE Trans. Neural Netw. Learn. Syst.*, pp. 1–13, 2020. [1, 2](#)
- [29] H. V. Nguyen, M. O. Ulfarsson, and J. R. Sveinsson, "Hyperspectral image denoising using sure-based unsupervised convolutional neural networks," *IEEE Trans. Geosci. Remote Sens.*, pp. 1–14, 2020. [1, 2, 3](#)
- [30] O. Sidorov and J. Yngve Hardeberg, "Deep hyperspectral prior: Single-image denoising, inpainting, super-resolution," in *In Proc. IEEE Int. Conf. Comput. Vis. (ICCV) Workshops*, Oct 2019. [1](#)
- [31] M. Aharon, M. Elad, and A. Bruckstein, "K-SVD: An algorithm for designing overcomplete dictionaries for sparse representation," *IEEE Trans. Signal Process.*, vol. 54, no. 11, pp. 4311–4322, 2006. [2](#)
- [32] A. Buades, B. Coll, and J. . Morel, "A non-local algorithm for image denoising," in *Proc. IEEE Conf. Comput. Vis. Pattern Recognit. (CVPR)*, vol. 2, 2005, pp. 60–65 vol. 2. [2, 4](#)
- [33] K. Dabov, A. Foi, V. Katkovnik, and K. Egiazarian, "Image denoising by sparse 3-d transform-domain collaborative filtering," *IEEE Trans. Image Process.*, vol. 16, no. 8, pp. 2080–2095, 2007. [2, 4, 5, 6, 7, 8](#)
- [34] M. Maggioni, V. Katkovnik, K. Egiazarian, and A. Foi, "Nonlocal transform-domain filter for volumetric data denoising and reconstruction," *IEEE Trans. Image Process.*, vol. 22, no. 1, pp. 119–133, 2013. [2, 5, 6, 7, 8](#)
- [35] Y. Qian, Y. Shen, M. Ye, and Q. Wang, "3-d nonlocal means filter with noise estimation for hyperspectral imagery denoising," in *Proc. IEEE International Geoscience and Remote Sensing Symposium (IGARSS)*, 2012, pp. 1345–1348. [2](#)
- [36] Y. Qian and M. Ye, "Hyperspectral imagery restoration using nonlocal spectral-spatial structured sparse representation with noise estimation," *IEEE J. Sel. Topics Appl. Earth Observ. Remote Sens.*, vol. 6, no. 2, pp. 499–515, 2013. [2](#)
- [37] N. Qi, Y. Shi, X. Sun, and B. Yin, "Tensr: Multi-dimensional tensor sparse representation," in *Proc. IEEE Conf. Comput. Vis. Pattern Recognit. (CVPR)*, 2016, pp. 5916–5925. [2, 4](#)
- [38] Y. Chang, L. Yan, X. L. Zhao, H. Fang, Z. Zhang, and S. Zhong, "Weighted low-rank tensor recovery for hyperspectral image restoration," *IEEE Trans. Cybern.*, vol. 50, no. 11, pp. 4558–4572, 2020. [2](#)
- [39] Y. Zhao and J. Yang, "Hyperspectral image denoising via sparse representation and low-rank constraint," *IEEE Trans. Geosci. Remote Sens.*, vol. 53, no. 1, pp. 296–308, 2015. [2](#)
- [40] T. Xie, S. Li, and B. Sun, "Hyperspectral images denoising via non-convex regularized low-rank and sparse matrix decomposition," *IEEE Trans. Image Process.*, vol. 29, pp. 44–56, 2020. [2](#)
- [41] X. Cao, Y. Chen, Q. Zhao, D. Meng, Y. Wang, D. Wang, and Z. Xu, "Low-rank matrix factorization under general mixture noise distributions," in *In Proc. IEEE Int. Conf. Comput. Vis. (ICCV)*, 2015, pp. 1493–1501. [2](#)
- [42] X. Cao, Q. Zhao, D. Meng, Y. Chen, and Z. Xu, "Robust low-rank matrix factorization under general mixture noise distributions," *IEEE Trans. Image Process.*, vol. 25, no. 10, pp. 4677–4690, 2016. [2](#)
- [43] Q. Zhao, D. Meng, Z. Xu, W. Zuo, and Y. Yan, " $l_1$ -norm low-rank matrix factorization by variational bayesian method," *IEEE Trans. Neural Netw. Learn. Syst.*, vol. 26, no. 4, pp. 825–839, 2015. [2](#)



- [44] F. Xiong, J. Zhou, and Y. Qian, "Hyperspectral restoration via  $L_0$  gradient regularized low-rank tensor factorization," *IEEE Trans. Geosci. Remote Sens.*, vol. 57, no. 12, pp. 10 410–10 425, 2019. [2](#)
- [45] X. Gong, W. Chen, and J. Chen, "A low-rank tensor dictionary learning method for hyperspectral image denoising," *IEEE Trans. Signal Process.*, vol. 68, pp. 1168–1180, 2020. [2](#)
- [46] Y. Fu, Y. Zheng, I. Sato, and Y. Sato, "Exploiting spectral-spatial correlation for coded hyperspectral image restoration," in *Proc. IEEE Conf. Comput. Vis. Pattern Recognit.(CVPR)*, June 2016. [2](#)
- [47] Q. Xie, M. Zhou, Q. Zhao, D. Meng, W. Zuo, and Z. Xu, "Multispectral and hyperspectral image fusion by ms/hs fusion net," in *Proc. IEEE Conf. Comput. Vis. Pattern Recognit.(CVPR)*, June 2019. [2](#), [4](#)
- [48] Q. Huang, W. Zhu, Y. Zhao, L. Chen, Y. Wang, T. Yue, and X. Cao, "Multispectral image intrinsic decomposition via subspace constraint," in *Proc. IEEE Conf. Comput. Vis. Pattern Recognit.(CVPR)*, 2018, pp. 6430–6439. [2](#)
- [49] L. Zhuang and J. M. Bioucas-Dias, "Fast hyperspectral image denoising and inpainting based on low-rank and sparse representations," *IEEE J. Sel. Topics Appl. Earth Observ. Remote Sens.*, vol. 11, no. 3, pp. 730–742, 2018. [2](#), [3](#), [4](#), [5](#), [6](#), [7](#), [8](#)
- [50] J. M. Bioucas-Dias and J. M. P. Nascimento, "Hyperspectral subspace identification," *IEEE Trans. Geosci. Remote Sens.*, vol. 46, no. 8, pp. 2435–2445, 2008. [3](#), [4](#)
- [51] H. Wang, Q. Xie, Q. Zhao, and D. Meng, "A model-driven deep neural network for single image rain removal," in *Proc. IEEE Conf. Comput. Vis. Pattern Recognit.(CVPR)*, June 2020. [4](#)
- [52] Y. Li, M. Tofighi, J. Geng, V. Monga, and Y. C. Eldar, "Efficient and interpretable deep blind image deblurring via algorithm unrolling," *IEEE Transactions on Computational Imaging*, vol. 6, pp. 666–681, 2020. [4](#)
- [53] J. Liu and X. Chen, "Alista: Analytic weights are as good as learned weights in lista," in *Proc. International Conference on Learning Representations (ICLR)*, 2019. [5](#)
- [54] D. Simon and M. Elad, "Rethinking the csc model for natural images," in *Proc. Advances in Neural Information Processing Systems (NeurIPS)*, 2019, pp. 2274–2284. [5](#)
- [55] L. Bruno, P. Jean, and K. Mairal, "Fully trainable and interpretable non-local sparse models for image restoration," In *Proc. European Conf.Comput. Vis. (ECCV)*, 2020. [5](#)